Maeda *et al. Earth, Planets and Space (2019) 71:94*
https://doi.org/10.1186/s40623-019-1073-z

Earth, Planets and Space

FULL PAPER Open Access

Causes of the N–S compressional aftershocks of the E–W compressional 2008 Iwate–Miyagi Nairiku earthquake (M7.2) in the northeastern Japan arc

Sumire Maeda[1*], Toru Matsuzawa[2], Keisuke Yoshida[2], Tomomi Okada[2] and Takeyoshi Yoshida[2]

Abstract

In this study, we investigated the influence of local structural heterogeneities on aftershocks of the 2008 Iwate–Miyagi Nairiku earthquake (M 7.2) that occurred in the northeastern Japan arc. Although this area is characterized by an E–W compressional thrust faulting stress regime, many N–S compressional thrust-type and strike-slip-type earthquakes were also observed in the aftershock activity of the 2008 event. The occurrence of such N–S compressional aftershocks indicates that the differential stress was very low before the main shock. We investigated V_p/V_s structure in the aftershock area in detail to find most of the area showed V_p/V_s as low as less than 1.70, which is consistent with the previous studies. Our result shows, however, the aftershock area was dotted with high V_p/V_s small areas, which suggests the locations of abundant fluid-filled cracks. The comparison of the distributions of V_p/V_s, the stress changes due to the mainshock, and focal mechanisms of the aftershocks indicate that the N–S compressional aftershocks are concentrated in regions with high V_p/V_s and large N–S compressional stress change. From these results, we concluded that the N–S compressional aftershocks occurred in regions with low strength due to the high pore pressure and with N–S compressional stress caused by the stress change due to the mainshock in a low differential stress regime.

Keywords: Microearthquakes, Stress field, Heterogeneous structure, Fluid, Geological structure

Introduction

The spatial distribution and focal mechanisms of inland earthquakes provide important insight into local structural heterogeneities (e.g., fluid, lithology, stress field, temperature, weak planes) in the crust (e.g., Magistrale and Zhou 1996; Umino et al. 1998; Hardebeck and Hauksson 1999; Maeda et al. 2018; Hauksson and Meier 2019). Earthquakes with fault types very different from those expected from the regional stress field have been reported by many researchers (e.g., Terakawa et al. 2013; Yoshida et al. 2014b; Vavryčuk and Adamová 2018). Causes of such strange earthquakes are usually attributed to the stress rotations due to large earthquakes or complex fault distributions. These phenomena also indicate that the maximum shear stress is not much larger than the stress drops of earthquakes there. Maeda et al. (2018) showed that microearthquake faulting styles in northwestern Kii Peninsula, southwestern Japan, can vary across a small region, indicating the crustal strength is very low in the region. These results indicate that the earthquakes do not necessarily occur in large differential stress regimes but rather in weak regions. Thus, it is very important to investigate the relations among the distributions of earthquakes, stress and structures to understand the inland earthquake generation mechanisms.

The Iwate–Miyagi Nairiku earthquake with a Japan Meteorological Agency (JMA) magnitude (Mj) of 7.2 occurred in the northeastern Japan arc on 14 June 2008 (Fig. 1) and was followed by numerous aftershocks. According to Terakawa and Matsu'ura (2010), this region

*Correspondence: maeda.sumire@aist.go.jp
[1] Geological Survey of Japan, National Institute of Advanced Industrial Science and Technology, AIST Tsukuba Central, 7, Higashi-1-1-1, Tsukuba, Ibaraki 305-8567, Japan
Full list of author information is available at the end of the article

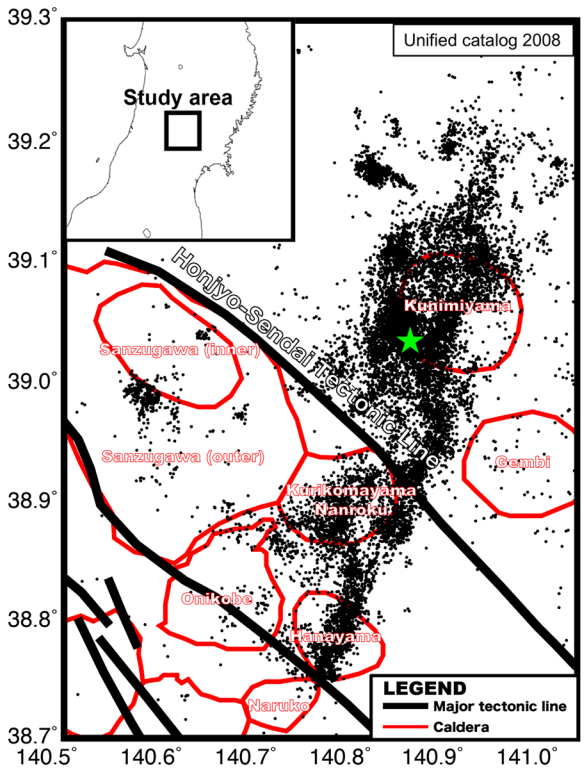

Fig. 1 Distribution of calderas, tectonic lines, and earthquakes in the study area. Calderas and tectonic lines are from Nunohara et al. (2010) and Baba (2017), respectively. Epicenters of earthquakes in 2008 at depths ≤ 15 km are shown as black dots and are from the JMA unified catalog. The green star denotes the mainshock epicenter estimated by Okada et al. (2012)

is located in a stress regime dominated by E–W compression, which also corresponds to the faulting style of the 2008 mainshock. However, many thrust-type earthquakes with N–S compression were identified as aftershocks of the 2008 event (Yoshida et al. 2014b). These exceptional aftershocks are concentrated in a region much narrower than the N–S compressional stress field predicted from the mainshock source model of Iinuma et al. (2009), which indicates that the distribution of these "exceptional" aftershocks is controlled not only by stress distribution but also by the strength distribution.

Immediately after the mainshock, the Group for the Aftershock Observations of the Iwate–Miyagi Nairiku Earthquake deployed a dense temporary seismic network in and around the focal area (Okada et al. 2012). Aftershock distribution and seismic velocity structure were investigated in detail. Okada et al. (2010, 2012, 2014) revealed that aftershocks occurred mainly in a shallow high-velocity zone overlying a low-velocity zone and interpreted this as a brittle zone overlying a fluid-rich area. If the earthquakes were caused by high pore fluid pressure due to the fluid provided from below, the ratio of *P*- and *S*-wave velocities (V_p/V_s) is expected to be higher there than in the surrounding area if the fluid was intruding in cracks (Takei 2002).

In this study, we investigate the relations among the distributions of V_p/V_s, stress change due to the 2008 event and its aftershocks. Our study is composed of the following three steps: First, we examine the distribution of aftershocks of the 2008 Iwate–Miyagi Nairiku earthquake and their faulting styles in detail. Second, we estimate a fine-scale V_p/V_s distribution in the aftershock area using a method proposed by Lin and Shearer (2007), which has higher resolution for regions with dense seismicity than usual seismic tomography methods. We discuss the relationship between the N–S compressional aftershocks of the 2008 earthquake and the inhomogeneous V_p/V_s structure in the last step.

Data and methods

Hypocenter and focal mechanism data

We combined the focal mechanism solutions of Yoshida et al. (2014b) with the precise hypocenters relocated by Okada et al. (2012) to investigate the characteristics of the focal mechanism distribution in detail.

Yoshida et al. (2014b) conducted a detailed analysis of regional hypocenters and focal mechanisms of earthquakes ($M_j > 1.0$) that occurred between 1996 and 2010. They relocated hypocenters by applying the double-difference (DD) location method (Waldhauser and Ellsworth 2000) and determined focal mechanism solutions using the HASH program (Hardebeck and Shearer 2002), adding newly picked *P*-wave first-motion data and using the one-dimensional velocity model of Hasegawa et al. (1978).

Okada et al. (2012) determined three-dimensional seismic velocity structure and relocated hypocenters simultaneously using the double-difference (DD) tomography method (Zhang and Thurber 2003) with data from a dense temporary observation network deployed in the study area. The one-dimensional (1D) velocity structure of Hasegawa et al. (1978) was used as their initial model. They analyzed earthquakes within the magnitude range of $1.0 \leq M_j \leq 5.7$ that occurred between 14 June 2008 and 30 September 2008, ending 3 months after the mainshock. The double-difference tomography method has the advantage of combining picked absolute arrival times with precise relative arrival times obtained from waveform analysis. As a result, this method can produce a more accurate velocity model and hypocenter distribution than standard tomography methods when hypocenters are densely distributed (Zhang and Thurber 2003). In addition, the hypocenters relocated by Okada et al. (2012) are considered well located due to a good station

coverage during the period of temporary aftershock observation (Yoshida et al. 2014b). Moreover, the DD tomography method can estimate the absolute locations of hypocenters, while DD relocation with a 1D structural model can only obtain precise relative locations. We, therefore, used the focal mechanisms determined by Yoshida et al. (2014b) combined with the precise hypocenter locations of Okada et al. (2012). In combining the two catalogs, we treat two hypocenters from respective catalogs as the same if differences of the origins of the two events are less than 0.5 s and 0.01° in time and space (both in latitude and longitude), respectively.

Focal mechanism solutions are classified as normal, strike-slip, or reverse types using the same scheme as Maeda et al. (2018), who introduced two grades (A and B) for each fault type: grade A means that a focal mechanism has an axis with a plunge angle $\theta \geq 60°$, and grade B indicates a plunge angle $45° \leq \theta < 60°$. We classified focal mechanisms satisfying neither criterion (i.e., $\theta < 45°$ for all axes) into a group labeled "other". We find not only E–W compressional-type events, as expected from the regional stress field (Terakawa and Matsu'ura 2010), but also N–S compressional-type aftershocks. To clarify the distribution of these exceptional aftershocks, we divided reverse fault-type and strike-slip fault-type events into N–S and E–W compressional subtypes: focal mechanisms with *P*-axes oriented within 30° of N–S (i.e., $0° \pm 30°$ or $180° \pm 30°$) were regarded as N–S compressional; others were regarded as E–W-compressional. Note that the range of orientations for the N–S compressional *P*-axes is much narrower than that for the E–W subclass because we would like to select N–S compressional events that cannot be treated as E–W compressional ones even when accounting for possible orientation uncertainty. Thus, we classified focal mechanisms into 11 subtypes: four subtypes of reverse faulting, four strike-slip, two normal fault subtypes, and one for "other".

Focal mechanisms could change slightly if we use the three-dimensional (3D) velocity model estimated by Okada et al. (2012). However, the focus of our concern here is the group of N–S-compressional focal mechanisms; such focal mechanisms cannot change to E–W compression with any physically plausible velocity model. Thus, we use the focal mechanisms of Yoshida et al. (2014b) without applying further corrections.

Estimation of V_p/V_s ratios

To investigate the relation between the aftershock activity and existence of fluid, we estimated the V_p/V_s distribution using the method proposed by Lin and Shearer (2007). This method is basically the same as computing a Wadati diagram, but can estimate local V_p/V_s ratios within a cluster of similar earthquakes using precise differential *P* and *S* arrival times obtained from waveform cross-correlation, yielding a resolution better than that obtained using usual tomographic methods (e.g., Lin and Shearer 2009).

As a preliminary step, we calculated waveform cross-correlations to improve the accuracy of arrival time differences. We used 16,332 earthquakes from the JMA unified earthquake catalog, located in the aftershock area of the 2008 Iwate–Miyagi Nairiku earthquake for the period from 14 June 2008 to 14 June 2009. We applied a 5–12-Hz bandpass filter to the 100-Hz sampling seismograms and computed cross-correlation functions for all the event pairs with epicentral separations less than 1.0 km. We used differential arrival times for hypocenter relocation whose waveforms show the cross-correlation coefficients larger than 0.8. The time lag of the absolute maximum of each cross-correlation function was initially computed at the original 100 Hz sampling rate. We then interpolated the waveform data with a quadratic function to obtain a precise lag time with an accuracy of ~ 1 ms, as in Shelly et al. (2013). We adopted durations of 2.5 and 4.0 s for the *P*- and *S*-wave windows, respectively, starting 0.3 s before respective phase onsets. *P*-wave windows were truncated to avoid contamination by *S*-wave energy for seismograms with *S*–*P* times less than 2.5 s (Yoshida and Hasegawa 2018). As a result, 1,315,244 differential arrival times were obtained.

Next, we applied the method of Lin and Shearer (2007) to the differential arrival times. Figure 2a illustrates the conceptual relationship between *P* differential travel time (δT_p) and *S* differential travel time (δT_s) for a pair of earthquakes observed at several stations. The data are plotted along a line whose slope represents the V_p/V_s ratio between the two hypocenters of the event pair when no errors are included. Since we do not know the correct travel times for real earthquakes, we have to use travel times (T_p and T_s) calculated from the differences between observed arrival times (t_p and t_s) and the calculated origin time (t_o):

$$T_p = t_p - t_o, \tag{1}$$

$$T_s = t_s - t_o. \tag{2}$$

Then, the differential travel times can be expressed as

$$\delta T_p = \delta t_p - \delta t_o, \tag{3}$$

$$\delta T_s = \delta t_s - \delta t_o, \tag{4}$$

where δt_p, δt_s, and δt_o represent differences in *P*-wave arrival times, *S*-wave arrival times, and origin times for an earthquake pair, respectively.

If we plot data from several event pairs in a compact earthquake cluster, the result should resemble the illustration in Fig. 2b. The data are distributed along many parallel

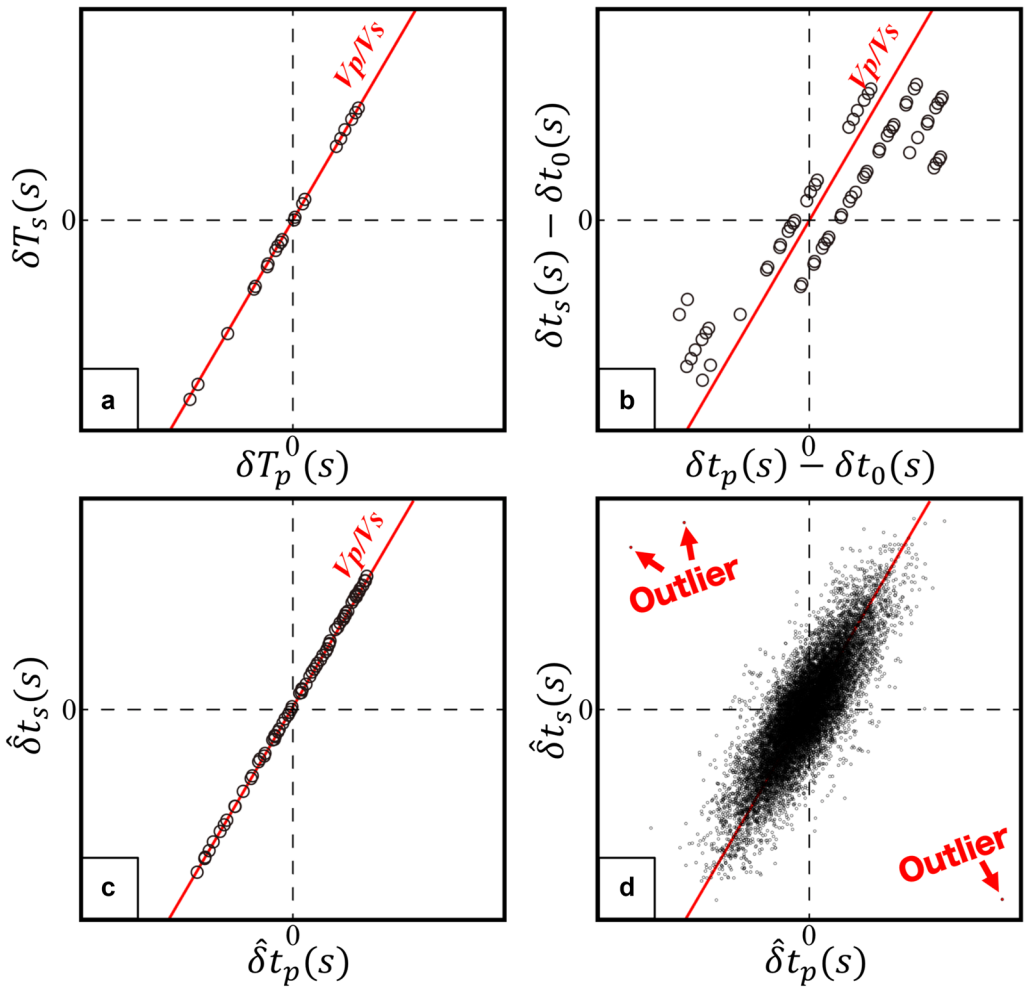

Fig. 2 Conceptual diagram of the method proposed by Lin and Shearer (2007). **a** *P* vs. *S* differential travel times for a single pair of events. **b** Synthetic *P* vs. *S* differential arrival times for several pairs of events in a compact cluster. **c** Distribution of differential arrival times after shifting the data shown in (**b**) so that they are aligned along a line crossing the origin, using the average values of respective event pairs for alignment. The slope of the line represents the local V_p/V_s ratio for the cluster. **d** Example of real data distribution after Lin and Shearer (2007). Outliers are indicated by red arrows and text

lines; each line corresponds to data from one pair of earthquakes at multiple stations. The slope of each line is the V_p/V_s ratio within the earthquake cluster. The offsets seen in Fig. 2b are due to uncertainties in differential origin times (δt_0). Lin and Shearer (2007) showed that these offsets can be canceled, as shown in Fig. 2c, if we plot "de-meaned" differential arrival times instead of the differential travel times estimated from Eqs. (3) and (4). This is because the de-meaned differential arrival times ($\widehat{\delta t}_p^i$ and $\widehat{\delta t}_s^i$), as defined by

$$\widehat{\delta t}_p^i \equiv \delta t_p^i - \delta \bar{t}_p, \tag{5}$$

$$\widehat{\delta t}_s^i \equiv \delta t_s^i - \delta \bar{t}_s, \tag{6}$$

satisfy

$$\widehat{\delta t}_s^i = \left(\frac{V_P}{V_S}\right) \widehat{\delta t}_p^i, \tag{7}$$

where δt_P^i and δt_s^i are the differential P and S arrival times for an event pair at station i, respectively; and $\delta \bar{t}_P$ and $\delta \bar{t}_s$ are the mean values of the differential arrival times from all stations for the event pair. Equation (7) indicates that if we plot de-meaned differential arrival times ($\widehat{\delta t}_p^i$, $\widehat{\delta t}_s^i$), then the data should be distributed along a line crossing the coordinate origin with a slope equal to the V_p/V_s ratio. In this way, we can estimate the local V_p/V_s ratio from all event pairs in the cluster (Lin and Shearer 2007). In principle, this provides a local measure of the average V_p/V_s within a cluster, which is typically only a few kilometers across (Lin and Shearer 2009). In this study, we divide

the region into many bins and estimate the V_p/V_s ratio in each bin using the earthquakes located within it. The size of each bin is fixed at 1.5 km × 1.5 km × 1.5 km, taking the hypocenter density, expected differential arrival times and typical estimation errors into consideration.

The differential arrival times estimated from the cross-correlation of the seismic waveforms may have large estimation errors due to the mismatching of the phases by one cycle which is known as "cycle skipping." This phenomenon occurs only when the pass-band of the filter is too narrow. Since we use here a rather wide pass-band of 5–12 Hz, such phenomenon is hard to occur. If the corner frequency of an earthquake is lower than 5 Hz (~0.2 s) and attenuation is very strong; however, the resultant filtered waveform might be monochromatic with a dominant frequency of 5 Hz. In this case, the differential arrival times might differ from the others by one cycle (about 0.2 s) or larger. Even if such cycle skipping occurs, the data will be removed as an outlier as shown in Fig. 2d because the error is much larger than usual estimation error. We calculated the mean μ and standard deviation *std* for each set of *P* and *S* differential arrival times and excluded values outside the $\mu \pm 3$std range. Finally, we recalculated the average values of the *P* and *S* differential arrival times.

After removing outliers, we superimposed data from many event pairs located in each bin and estimated the V_p/V_s ratio in each bin from the slope of the distribution using principal components analysis (PCA) (e.g., Pearson 1901; Hotelling 1933). By applying PCA to our two-dimensional data set, we obtain two principal component vectors and their respective eigenvalues λ. We estimated the V_p/V_s ratio for each bin from the inclination of the eigenvector with the largest eigenvalue. Since each eigenvalue is proportional to the width of the distribution in the direction of the corresponding eigenvector, the ratio of two eigenvalues can be used as an indicator of the reliability of the estimated V_p/V_s value. When the event cluster size is too small or the station separation is too narrow, the eigenvalue ratio tends to become as small as 1.0 and the estimated V_p/V_s ratio is unreliable. To evaluate the reliability of the obtained V_p/V_s ratio, we used the bootstrap method of Efron (1987): in each bin, we carried out bootstrap resampling 100 times and calculated the V_p/V_s ratio of the resampled data using the standard deviation std_b of the bootstrap results as the standard error of V_p/V_s. We retained estimates with $\mathrm{std}_b \leq 0.1$ and eigenvalue ratios $\lambda_1/\lambda_2 \geq 10.0$ for further analyses.

Then, we shifted the bins horizontally by 0.005 degrees and vertically by 1.0 km, and estimated the V_p/V_s for each bin using the same procedure as described above and superimpose those sets of results to investigate the detailed but smoothed V_p/V_s distribution.

Results

Focal mechanism distribution

Distributions of focal mechanisms corresponding to individual fault types are shown in Fig. 3, and cross sections are shown in Fig. 4. Reverse or strike-slip aftershocks with E–W compression are dominant. Figure 3a indicates that most reverse-fault earthquakes with the E–W compression distribute in the NNE–SSW direction, and they can be further subdivided into northern and southern clusters as indicated by two dashed-line ovals. On the other hand, N–S compressional thrust-type earthquakes are concentrated around the center of the aftershock area, comprising a cluster in the NNW–SSE direction (Fig. 3b). Note that they are distributed as if they connect two clusters of E–W A-type reverse-fault earthquakes (RAEW).

Okada et al. (2012) showed that the aftershocks include westward- and eastward-dipping clusters, which were previously interpreted as mutually conjugate faults. InSAR and tilt data also support this interpretation (Takada et al. 2009; Fukuyama 2015). Figure 4 shows that thrust-type earthquakes dominated by E–W compression similar to the mainshock dominate the westward-dipping cluster, which probably represents the source fault of the mainshock. The eastward-dipping cluster contains many thrust-type earthquakes with N–S compression, but many E–W compressional thrust earthquakes also occur in this cluster within the hanging wall of the suspected mainshock fault. Strike-slip earthquakes seem to be concentrated around the intersection of the two dipping clusters of reverse-fault earthquakes in Fig. 4.

V_p/V_s distribution

The distributions of estimated V_p/V_s ratios with errors $std_b \leq 0.1$ and eigenvalue ratios $\lambda_1/\lambda_2 \geq 10.0$ are shown in Fig. 5. Only 958 of 8357 bins with earthquake data met these reliability criteria. The average value of V_p/V_s across all reliable bins is 1.63 and the frequency distribution is shown in Fig. 6a; most ratios in this region lie within the range $1.45 \leq V_p/V_s \leq 1.80$. Examples of the data distributions of this study are shown in Fig. 6b–d. The depth ranges of bins are 0.00–1.50, 0.75–2.25, 1.50–3.00, 2.25–3.75, 3.00–4.50, 3.75–5.25, 4.50–6.00, 5.25–6.75, 6.00–7.50, 6.75–8.25, 7.50–9.00, and 8.25–9.75 km. The estimated minimum, average, and maximum values of the V_p/V_s ratios in different depth ranges are listed in Table 1.

Figure 5 shows that V_p/V_s ratios were estimated only in the Hanayama caldera at the southern end of the aftershock area (Fig. 1) in the shallowest depth range (0.00–1.50 km). In 0.75–2.25 km depth range, V_p/V_s ratios were estimated close to the northern and southern ends of the

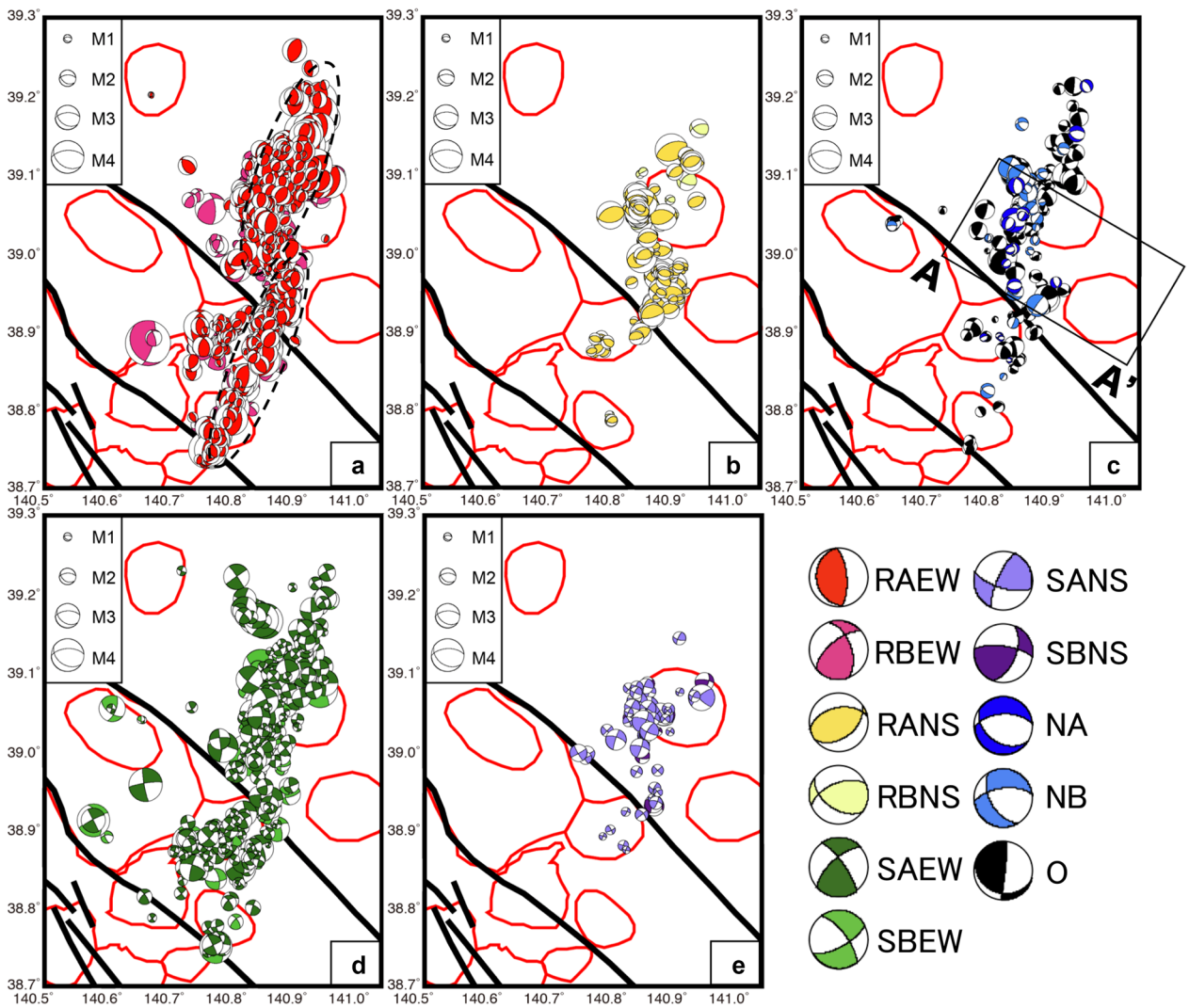

Fig. 3 Focal mechanism distributions. Focal mechanisms of earthquakes for the period from 14 June 2008 to 30 September 2008 are shown. **a** Distribution of reverse-faulting events with E–W compression composing subgroups A (RAEW) and B (RBEW). Dashed black ellipses indicate northern and southern clusters. **b** Distribution of reverse-faulting events with N–S compression composing subgroups A (RANS) and B (RBNS). **c** Distribution of normal-faulting events composing subgroups A (NA) and B (NB), and other events (O). The black rectangle indicates the location of the cross sections in Fig. 4. **d** Distribution of E–W-compressional strike-slip events composing subgroups A (SAEW) and B (SBEW). **e** Distribution of N–S-compressional strike-slip events composing subgroups A (SANS) and B (SBNS)

aftershock area. The southern end of V_p/V_s values shows $V_p/V_s < 1.70$, while both low and high V_p/V_s ratios appear in the northern end. In ranges of 1.50–3.00, 2.25–3.75, 3.00–4.50, 3.75–5.25, 4.50–6.00 and 5.25–6.75 km, V_p/V_s ratios were estimated between the Kurikomayama Nanroku caldera and the Kunimiyama caldera (Mizuyama caldera by Osozawa and Nunohara 2013) and they are considerably inhomogeneous. In ranges of 3.00–4.50 and 3.75–5.25 km, exceptionally high V_p/V_s ratios seem to be located near the main shock. In ranges of 3.75–5.25, 4.50–6.00, 5.25–6.75, 6.00–7.50, 6.75–8.25 and 7.50–9.00 km, V_p/V_s values are generally estimated less than 1.70 inside the Kunimiyama caldera, but several bins of high V_p/V_s are located adjacent to the bins with low V_p/V_s. In 8.25–9.75 km depth range, V_p/V_s ratios are close to 1.70.

Discussion

Low-V_p/V_s regions in the aftershock area

As shown in the previous section, V_p/V_s ratios estimated using the method of Lin and Shearer (2007) in the study area show V_p/V_s values of 1.45–1.80 over a

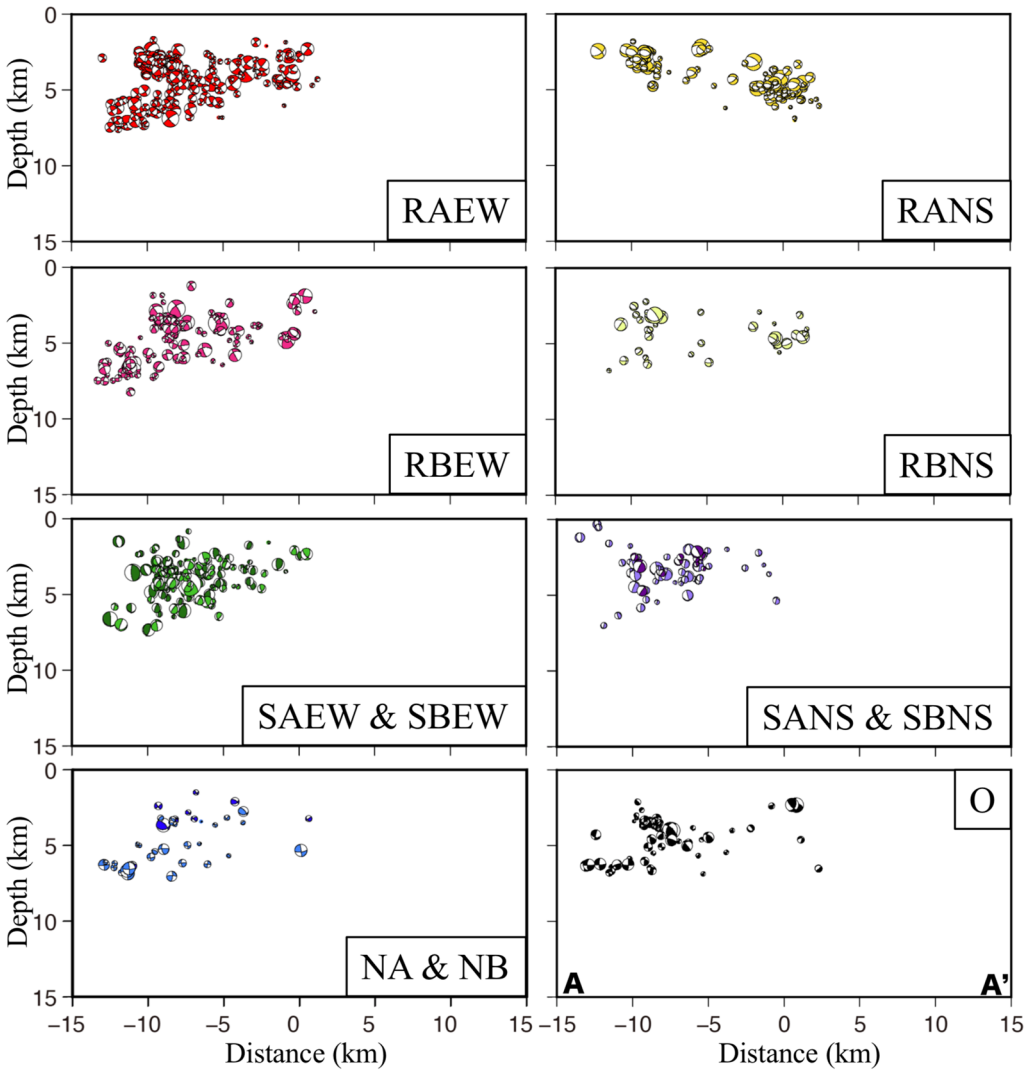

Fig. 4 Cross sections of focal mechanism distributions. Focal mechanisms of earthquakes in the black rectangle in Fig. 3c are projected onto the plane *A*–*A*′. See the caption of Fig. 3 and the text for the classification of focal mechanisms

wide range of the aftershock area (Figs. 5, 6). Most of the values are much smaller than 1.73 (Poisson's ratio of 0.25), which is often assumed to be the average or expected value of V_p/V_s. Many previous studies have confirmed that V_p/V_s in seismogenic zones in the upper crust is often less than 1.70 (e.g., Hashida and Ukawa 1997; Nakajima et al. 2001; Kato et al. 2005; Matsubara et al. 2008; Okada et al. 2012; Jo and Hong 2013; Okada et al. 2014; Yukutake et al. 2015). In particular, Nakajima et al. (2001) and Okada et al. (2012, 2014) reported that V_p/V_s in the aftershock area of the Iwate–Miyagi Nairiku earthquake was basically less than 1.70. Yukutake et al. (2015) estimated V_p/V_s around Hakone volcano using the method of Lin and Shearer (2007) and found values as low as $V_p/V_s = 1.58 \pm 0.07$ above the magma source. Hashida and Ukawa (1997) investigated the upper crust of the Kanto–Tokai region, Japan, and obtained V_p/V_s ratios less than 1.70 in southern Nagano Prefecture, northern Kanto district, and Izu Peninsula.

One reason why low V_p/V_s ratios dominate in these regions is thought to be the influence of the mineral composition of rocks constituting the upper crust. According to the measurement of Christensen (1996), Granite–granodiorite shows V_p/V_s ratios of 1.70 at 200 MPa. Basement rocks in the aftershock area of this study are granitoids (Sasada 1985), and thus, their V_p/V_s ratios are expected to be ~ 1.70. Christensen (1996) also showed $V_p/V_s = 1.48$ for quartzite at 200 MPa.

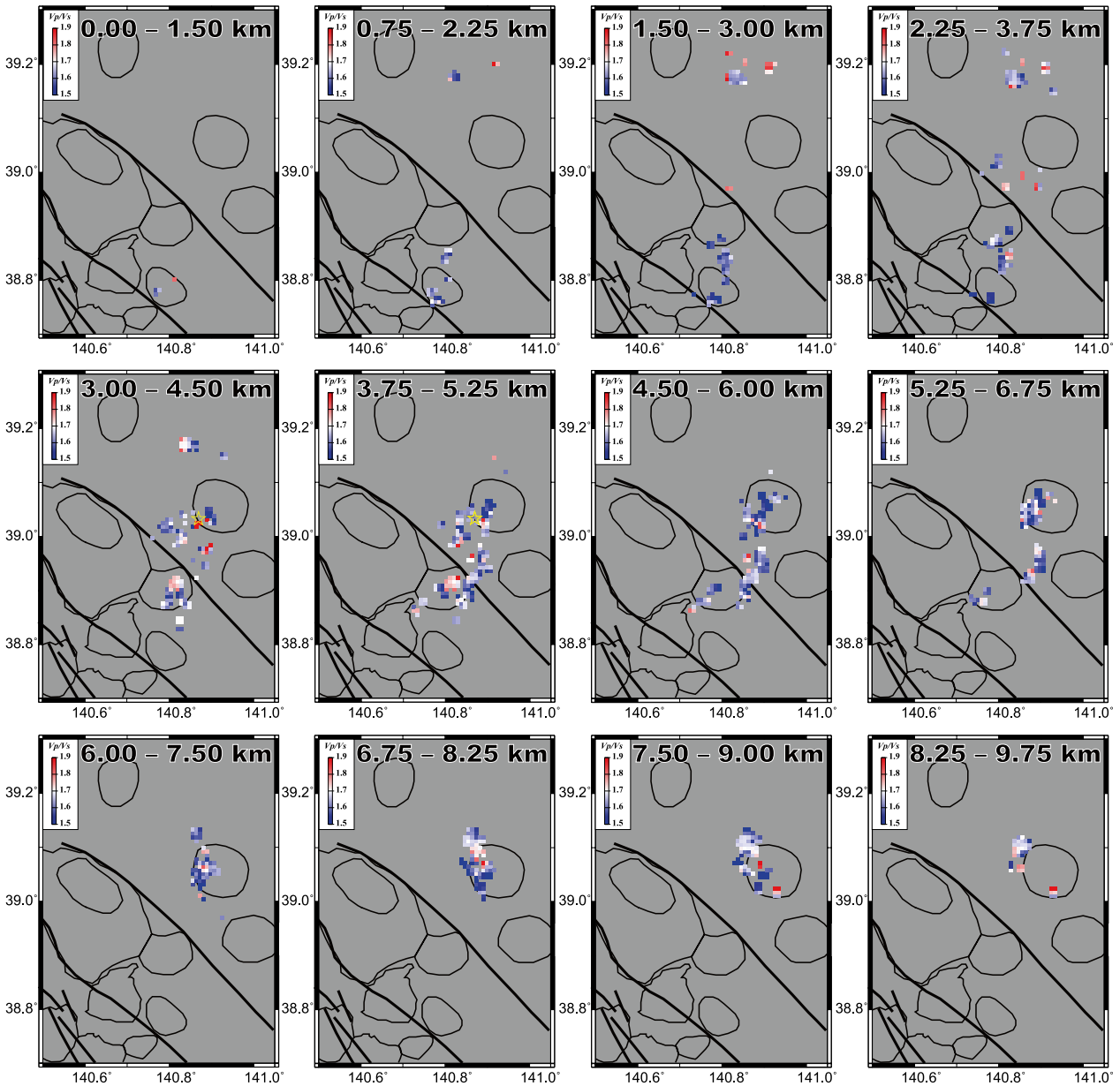

Fig. 5 V_p/V_s distribution estimated in this study. The yellow star denotes the mainshock epicenter estimated by Okada et al. (2012). See the caption of Fig. 1 and the text for calderas and tectonic lines

Therefore, if quartz is abundant in the area, or quartz veins are developed in granitic basement rocks, the V_p/V_s ratios are expected to be less than 1.70.

Sasada (1984, 1985) clarified the chemical composition of granitoid in pre-Neogene basement rocks around Mt. Kurikoma in the present study area: many rock samples are tonalite that are poor in K-feldspar and rich in quartz (generally larger than 25%vol., but up to 35%vol.) (Additional file 1: Figure S1). Their quartz-rich samples are taken from regions that correspond to the low-V_p/V_s regions estimated in this study, while samples with quartz contents of < 25% seems to be distributed in the region of high V_p/V_s ratios revealed by Okada et al. (2012) (Additional file 1: Figure S2).

A low V_p/V_s value can be also explained by fluid in granular (equilibrium geometry) or tube-shaped pores in rocks (Takei 2002). In the remarkable low-V_p/V_s region estimated by Okada et al. (2012), however, *Vs* is higher than in the surrounding areas. The tomography results of Nakajima et al. (2001) also show that V_p/V_s in

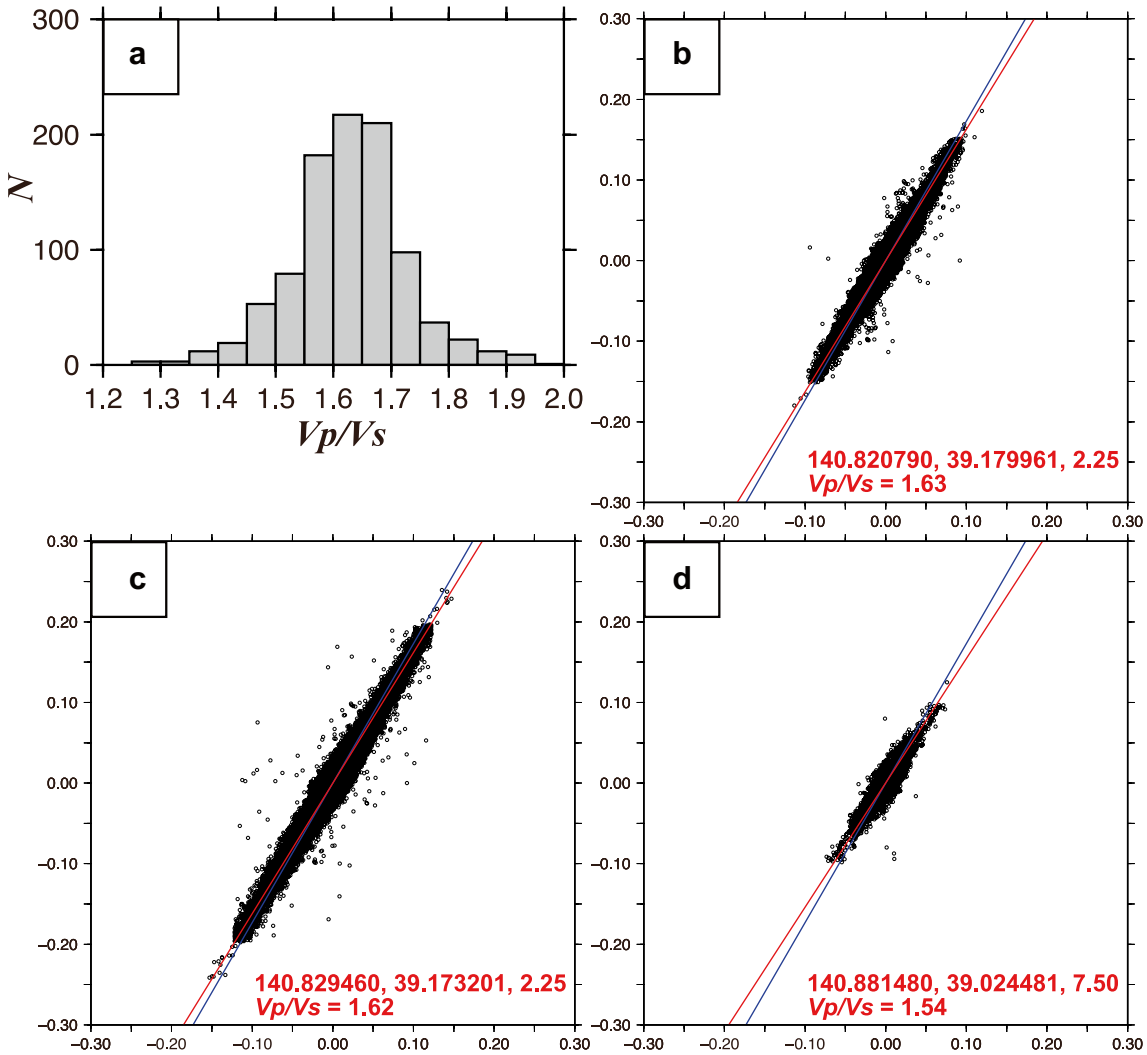

Fig. 6 **a** Histogram of V_p/V_s ratios estimated in this study and **b**–**d** examples of the data distributions. Slope of the red line represents the local V_p/V_s ratio for the cluster. Blue line is drawn as a reference whose slope is 1.73. Red texts represent the center of the longitude, latitude and depth ranges, and V_p/V_s ratio for the corresponding data

this study area is lower and *Vs* is higher than in the surrounding area. If the basement rocks contain significant fluid, *Vs* would be relatively low. Therefore, it is difficult to explain the low V_p/V_s ratios in this study area with the presence of fluid.

In measurements made by Christensen (1996) at 200 MPa pressure, the *P*- and *S*-wave velocities of granite–granodiorite are 6.2 km/s and 3.7 km/s, respectively. The *P*-wave velocity of quartzite is estimated to be 6.0 km/s (i.e., slower than granite–granodiorite), while the *S*-wave velocity is 4.0 km/s. Therefore, a quartz-rich model can explain the low V_p/V_s and high *Vs* in the aftershock area of the Iwate–Miyagi Nairiku earthquake.

Relationship between *Vp/Vs* and earthquake generation

The results of this study show that low V_p/V_s dominates the aftershock area of the Iwate–Miyagi Nairiku earthquake. The method of Lin and Shearer (2007), however, cannot estimate V_p/V_s in regions without earthquakes. Thus, it is not resolved whether the low V_p/V_s region is limited to the aftershock area or extends throughout the upper crust. Therefore, it is necessary to compare our results with the results of tomography to estimate the extent of the low V_p/V_s region resolved by the present work.

Nakajima et al. (2001) investigated *P*- and *S*-wave velocities in the Tohoku district (northeastern Honshu, Japan) and computed V_p/V_s ratios, yielding an averaged

Table 1 Minimum, average, and maximum V_p/V_s ratios in different depth ranges

	Minimum	Average	Maximum
0.00–1.50 km	1.57	1.66	1.81
0.75–2.25 km	1.51	1.63	1.93
1.50–3.00 km	1.37	1.64	2.03
2.25–3.75 km	1.36	1.64	1.86
3.00–4.50 km	1.31	1.65	1.99
3.75–5.25 km	1.28	1.63	1.93
4.50–6.00 km	1.30	1.61	1.86
5.25–6.75 km	1.39	1.62	1.81
6.00–7.50 km	1.40	1.61	1.82
6.75–8.25 km	1.38	1.61	1.88
7.50–9.00 km	1.33	1.63	1.93
8.25–9.75 km	1.51	1.68	1.93

V_p/V_s of 1.69 for the upper crust in the Tohoku region and a value of ~ 1.70 at 10-km depth in the aftershock area of the Iwate–Miyagi Nairiku earthquake.

Okada et al. (2012) reported high-resolution cross sections of the V_p/V_s distribution in the aftershock area of the Iwate–Miyagi Nairiku earthquake computed from data of a dense temporary seismic observation network. Their cross sections confirm that V_p/V_s ratios of 1.61–1.70 are dominant in the aftershock area, although some regions have ratios as high as 1.90.

The present analysis has revealed that the area of the Iwate–Miyagi Nairiku earthquake have low V_p/V_s ratios, but $V_p/V_s > 1.90$ in some regions, which is consistent with the results of Okada et al. (2012). Those tomographic results show a gradual change from a region of low V_p/V_s to a region with high V_p/V_s, but the spatial resolution in their study was several kilometers or more. On the other hand, the results of our study suggest that high V_p/V_s ratios are confined to "spots" as shown in Fig. 5. From the results of the present and previous studies, it can be concluded that the upper crust in the region is dominated by V_p/V_s ratios less than 1.70. Moreover, our study indicates that seismogenic regions within the upper crust are heterogeneous, with V_p/V_s varying on length scales of several kilometers. The heterogeneity of these V_p/V_s values might be attributed to the presence of fluids, differences in rock types, or both.

Causes of the N–S-compressional aftershocks

The focal mechanism analysis of the present study shows that the westward-dipping planar aftershock distribution is dominated by E–W-compressional thrust earthquakes, while the eastward-dipping distribution contains many N–S-compressional thrust earthquakes as shown in Fig. 4. After the occurrence of a large thrust earthquake with E–W compression, N–S compressional stress is expected to increase in the area immediately east and west of the main rupture zone (Yoshida et al. 2014a). Therefore, if the E–W background compressive stress in the Tohoku district (e.g., Terakawa and Matsu'ura 2010) is not extremely large, aftershocks showing N–S compression are likely to occur east and west of the mainshock rupture area. However, the actual aftershocks that show reverse faulting with N–S compression are distributed forming a narrow eastward-tilting cluster. To verify whether this distribution can be attributed to heterogeneities in the stress or strength distributions, we quantitatively examine the distributions of focal mechanisms with N–S compression, stress field, and V_p/V_s ratios.

Figure 7 shows the distribution of V_p/V_s ratios estimated by Okada et al. (2012), the distribution of the N–S compression-type focal mechanisms (RANS, SANS) classified in this study, and the distribution of the axes of maximum compressive stress change due to the mainshock (herein, $\Delta\sigma_1$) estimated by Yoshida et al. (2014a). Large N–S compressional stress changes are observed both east and west of the aftershock area, corresponding to the hanging wall and footwall, respectively (see Additional file 1: Figure S2). Earthquakes dominated by N–S compression occur mainly in regions of $V_p/V_s \approx 1.70$, sandwiched between low-V_p/V_s regions to the west and high-V_p/V_s regions to the east. Both the results of our study in Fig. 5 and Okada et al. (2012) shown in Fig. 7 represent that V_p/V_s ratios are less than 1.70 in most of the aftershock area. Figure 7 also indicates that earthquakes with N–S compression occurred mainly in regions with $V_p/V_s \approx 1.70$, $\Delta\sigma_1$ axes oriented N–S, and differential stress changes > 8 MPa ($\log(\Delta\sigma_1 - \Delta\sigma_3) > 0.9$). There are no N–S compressional earthquakes in regions with $V_p/V_s < 1.70$, even if $\Delta\sigma_1$ axes were oriented N–S and differential stress change exceeded 8 MPa.

In the previous section, we showed that basement rocks in the upper crust of the northeastern Japan arc are generally characterized by $V_p/V_s < 1.70$. Takei (2002) pointed out that V_p/V_s increases when fluid-filled cracks are present. Therefore, the regions of the upper crust with $V_p/V_s > 1.70$ might correspond to fluid-rich portions.

Kato et al. (2005) discussed the relationship between the aftershocks of the 2004 Niigata–Chuetsu (mid-Niigata prefecture) earthquake and the velocity structure of the upper crust. They found that the aftershocks were distributed in a zone of low-to-moderate V_p/V_s ($1.65 \leq V_p/V_s \leq 1.75$), and a zone of significantly low V_p/V_s (< 1.65) coincides with the area where aftershock activity was low. They proposed that the low-V_p/V_s zone corresponds to old basement rock and the low-to-moderate-V_p/V_s zone could be explained by the presence of water-filled pores with high aspect ratios, based on the results of Takei (2002). From

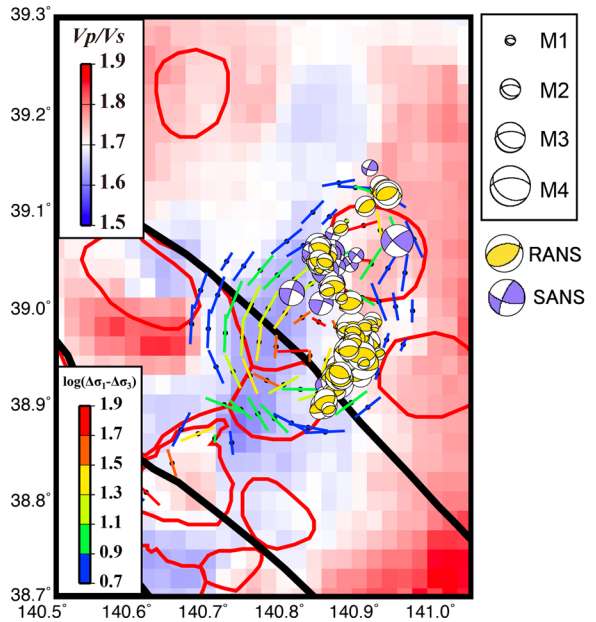

Fig. 7 Distribution of V_p/V_s ratios, events with N–S compression, and axes of maximum compressive stress change. Distribution of V_p/V_s at 4.5 km depth is from Okada et al. (2012). Focal mechanism solutions with N–S compression from category A events (RANS and SANS) in the depth range 3.25–6.25 km are shown. Bars represent axes of the maximum compressive stress changes ($\Delta\sigma_1$) caused by the mainshock at 5-km depth projected to the surface (Yoshida et al. 2014b). The color of each bar represents to the magnitude of the calculated differential stress change. Only differential stress changes $\geq$ 5 MPa are plotted. In the title of the bottom-left scale bar, "log" means the common (base 10) logarithm and the units are MPa. The value of 0.7 on the logarithmic scale corresponds to 5 MPa and 0.9 corresponds to 8 MPa

these observations, they suggest that the inhomogeneous distribution of pore water contributes to the generation of aftershocks. From the discussion above, we conclude that earthquakes with N–S compressive stress occurred only in regions where N–S compressional stress change caused by the mainshock was large and the strength was low owing to the abundance of fluids.

Conclusions

In this study, we investigated the influence of local structural heterogeneities in the upper crust on aftershocks of the 2008 Iwate–Miyagi Nairiku earthquake in the northeastern Japan arc. We found that the aftershock region is basically characterized by low V_p/V_s ratio probably due to the quartz-rich composition of rocks but the region is dotted with high V_p/V_s areas as small as several kilometers. The aftershocks are composing westward-dipping cluster and eastward-dipping cluster. While the former is dominated by reverse-fault-type earthquakes with E–W compression which is the same as the mainshock, many N–S compressional earthquakes are concentrated in space within the latter. These N–S compressional earthquakes occurred mainly in regions where $V_P/V_S \approx 1.70$, N–S compressional stress change was induced by the mainshock, and the change in the differential stress was larger than 8 MPa. There are no aftershocks with N–S compression in regions with $V_p/V_s < 1.70$, even if the expected N–S compressive stress change was large there. Thus, the N–S compressional aftershocks were probably generated by high pressure of pore fluids in addition to the N–S compressional stress change caused by the mainshock.

Supplementary information

Supplementary information accompanies this paper at https://doi.org/10.1186/s40623-019-1073-z.

Additional file 1. Additional figures.

Abbreviations

JMA: Japan Meteorological Agency; Mj: JMA magnitude; DD: double-difference; RAEW: reverse-fault A-type earthquake with E–W compression; RBEW: reverse-fault B-type earthquake with E–W compression; RANS: reverse-fault A-type earthquake with N–S compression; RBNS: reverse-fault B-type earthquake with N–S compression; SAEW: strike-slip-fault A-type earthquake with E–W compression; SBEW: strike-slip-fault B-type earthquake with E–W compression; SANS: strike-slip-fault A-type earthquake with N–S compression; SBNS: strike-slip-fault B-type earthquake with N–S compression; NA: normal-fault A-type earthquake; NB: normal-fault B-type earthquake; O: other type earthquake; PCA: principal components analysis.

Acknowledgements

We thank R. Takagi of Tohoku University and T. Kubota of the National Research Institute for Earth Science and Disaster Resilience for the valuable discussion. The authors thank the Lead Guest Editor J. Nakajima and the reviewers T. Yamada and an anonymous reviewer for their helpful comments, which have improved the manuscript. We used the unified earthquake catalog of the Japan Meteorological Agency (JMA). The figures in this paper were prepared using the Generic Mapping Tools (GMT) software package (Wessel and Smith 1998).

Authors' contributions

Data analysis and manuscript preparation were carried out mainly by SM. TM directed the study at all stages. KY analyzed the data to estimate accurate arrival time differences. KY and TO provided focal mechanism data and relocated hypocenters using the double-difference tomography method, respectively. TY participated in the design of the study and discussion. All authors read and approved the final manuscript.

Funding

This research was supported by JSPS KAKENHI Grant Number JP26109002.

Availability of data and materials

The datasets analyzed in this study are available from the corresponding author upon reasonable request.

Ethics approval and consent to participate

Not applicable.

Consent for publication

Not applicable.

Competing interests

The authors declare that they have no competing interests.

Author details
[1] Geological Survey of Japan, National Institute of Advanced Industrial Science and Technology, AIST Tsukuba Central, 7, Higashi-1-1-1, Tsukuba, Ibaraki 305-8567, Japan. [2] Graduate School of Science, Tohoku University, 6-6 Aza-Aoba, Aramaki, Aoba-ku, Sendai 980-8578, Japan.

Received: 10 May 2019 Accepted: 21 August 2019
Published online: 03 September 2019

References

Baba K (2017) Marine geology (Chapter 10). In: Geological Society of Japan (ed) Regional Geology of Japan 2, Tohoku District (Nihon Chiho Chishitsushi 2 Tohoku Chiho). Asakura Publishing Co. Ltd., pp 427–478 (**in Japanese**)

Christensen NI (1996) Poisson's ratio and crustal seismology. J Geophys Res 101(B2):3139–3156. https://doi.org/10.1029/95JB03446

Efron B (1987) Better bootstrap confidence intervals. J Am Stat Assoc 82(397):171–185. https://doi.org/10.1080/01621459.1987.10478410

Fukuyama E (2015) Dynamic faulting on a conjugate fault system detected by near-fault tilt measurements. Earth Planets Space 67(1):38. https://doi.org/10.1186/s40623-015-0207-1

Geological Survey of Japan, AIST (ed.) (2018) Seamless digital geological map of Japan 1:200,000

Hardebeck JL, Hauksson E (1999) Role of fluids in faulting inferred from stress field signatures. Science 285:236–239. https://doi.org/10.1126/science.285.5425.236

Hardebeck JL, Shearer PM (2002) A new method for determining first-motion focal mechanisms. B Seismol Soc Am 92(6):2264–2276. https://doi.org/10.1785/0120010200

Hasegawa A, Umino N, Takagi A (1978) Double-planed structure of the deep seismic zone in the northeastern Japan arc. Tectonophysics 47(1):43–58. https://doi.org/10.1016/0040-1951(78)90150-6

Hashida Y, Ukawa M (1997) Upper Crustal V_p/V_s ratios in Kanto-Tokai district, Japan. J Seismol Soc Japan 50:315–327 **(in Japanese with English abstract)**

Hauksson E, Meier M (2019) Applying depth distribution of seismicity to determine thermo-mechanical properties of the seismogenic crust in southern california: comparing lithotectonic blocks. Pure Appl Geophys 176:1061–1081. https://doi.org/10.1007/s00024-018-1981-z

Hotelling H (1933) Analysis of a complex of statistical variables into principal components. J Educ Psychol 24(6 & 7):417–441

Iinuma T, Ohzono M, Ohta Y, Miura S, Kasahara M, Takahashi H, Sagiya T, Matsushima T, Nakao S, Ueki S, Tachibana K, Sato T, Tsushima H, Takatsuka K, Yamaguchi T, Ichiyanagi M, Takada M, Ozawa K, Fukuda M, Asahi Y, Nakamoto M, Yamashita Y, Umino N (2009) Aseismic slow slip on an inland active fault triggered by a nearby shallow event, the 2008 Iwate–Miyagi Nairiku earthquake (Mw68). Geophys Res Lett 36:L20308. https://doi.org/10.1029/2009gl040063

Jo E, Hong TK (2013) VP/VS ratios in the upper crust of the southern Korean Peninsula and their correlations with seismic and geophysical properties. J Asian Earth Sci 66:204–214. https://doi.org/10.1016/j.jseaes.2013.01.008

Kato A, Kurashimo E, Hirata N, Sakai S, Iwasaki T, Kanazawa T (2005) Imaging the source region of the 2004 mid-Niigata prefecture earthquake and the evolution of a seismogenic thrust-related fold. Geophys Res Lett 32(7):1–4. https://doi.org/10.1029/2005gl022366

Lin G, Shearer P (2007) Estimating local V_p/V_s ratios within similar earthquake clusters. B Seismol Soc Am 97(2):379–388. https://doi.org/10.1785/0120060115

Lin G, Shearer PM (2009) Evidence for water-filled cracks in earthquake source regions. Geophys Res Lett 36(17):1–5. https://doi.org/10.1029/2009GL039098

Maeda S, Matsuzawa T, Toda S, Yoshida K, Katao H (2018) Complex microseismic activity and depth-dependent stress field changes in Wakayama, southwestern Japan. Earth Planets Space 70(1):21. https://doi.org/10.1186/s40623-018-0788-6

Magistrale H, Zhou HW (1996) Lithologic control of the depth of earthquakes in Southern California. Science 273:639–642. https://doi.org/10.1126/science.273.5275.639

Matsubara M, Obara K, Kasahara K (2008) Three-dimensional P- and S-wave velocity structures beneath the Japan Islands obtained by high-density seismic stations by seismic tomography. Tectonophysics 454:86–103. https://doi.org/10.1016/j.tecto.2008.04.016

Nakajima J, Matsuzawa T, Hasegawa A, Zhao D (2001) Three-dimensional structure of Vp, Vs, and V_p/V_s beneath northeastern Japan: implications for arc magmatism and fluids. J Geophys Res 106(B10):21843–21857. https://doi.org/10.1029/2000JB000008

Nunohara K, Yoshida T, Yamada R, Maeda S, Ikeda K, Nagahashi Y, Yamamoto A, Kudo T (2010) Geology and geologic structure around the area of hypocenter of the 2008 Iwate-Miyagi Nairiku earthquake. Earth Monthly 32:356–366 **(in Japanese)**

Okada T, Umino N, Hasegawa A (2010) Deep structure of the Ou mountain range strain concentration zone and the focal area of the 2008 Iwate–Miyagi Nairiku earthquake, NE Japan—seismogenesis related with magma and crustal fluid. Earth Planets Space 62:347–352. https://doi.org/10.5047/eps.2009.11.005

Okada T, Umino N, Hasegawa A (2012) Hypocenter distribution and heterogeneous seismic velocity structure in and around the focal area of the 2008 Iwate-Miyagi Nairiku Earthquake, NE Japan—possible seismological evidence for a fluid driven compressional inversion earthquake. Earth Planets Space 64:717–728. https://doi.org/10.5047/eps.2012.03.005

Okada T, Matsuzawa T, Nakajima J, Uchida N, Yamamoto M, Hori S, Kono T, Nakayama T, Hirahara S, Hasegawa A (2014) Seismic velocity structure in and around the Naruko volcano, NE Japan, and its implications for volcanic and seismic activities. Earth Planets Space 66:114. https://doi.org/10.1186/1880-5981-66-114

Osozawa S, Nunohara K (2013) Surface ruptures of the 2008 M 6.9 Iwate–Miyagi Nairiku earthquake at Ichinoseki City area: reverse fault reactivation of Late Miocene caldera-collapse normal faults overlapping a Middle Miocene listric normal fault. J Geol Soc Japan 119(Supplement):18–26 **(in Japanese)**

Pearson K (1901) On lines and planes of closest fit to systems of points in space. Philos Mag Ser 2(11):559–572

Sasada M (1984) The pre Neogene basement rocks of the Kamuro Yama Kurikoma Yama area, northeastern Honshu, Japan Part 1, Onikobe Yuzawa Mylonaite zone. J Geol Soc Japan 90(12):865–874 **(in Japanese with English abstract)**

Sasada M (1985) The pre Neogene basement rocks of the Kamuro Yama Kurikoma Yama area, Northeastern Honshu, Japan Part 2, Boundary between the Abukuma and Kitakami belts. J Geol Soc Japan 91(1):1–17 **(in Japanese with English abstract)**

Shelly DR, Moran SC, Thelen WA (2013) Evidence for fluid-triggered slip in the 2009 Mount Rainier. Washington earthquake swarm. Geophys Res Lett 40(8):1506–1512. https://doi.org/10.1002/grl.50354

Takada Y, Kobayashi T, Furuya M, Murakami M (2009) Coseismic displacement due to the 2008 Iwate-Miyagi Nairiku earthquake detected by ALOS/PALSAR: preliminary results. Earth Planets Space 61:e9–e12. https://doi.org/10.1186/BF03353153

Takei Y (2002) Effect of pore geometry on VP/VS: from equilibrium geometry to crack. J Geophys Res 107(B2):2043. https://doi.org/10.1029/2001JB000522

Terakawa T, Matsu'ura M (2010) The 3-D tectonic stress fields in and around Japan inverted from centroid moment tensor data of seismic events. Tectonics 29:TC6008. https://doi.org/10.1029/2009tc002626

Terakawa T, Hashimoto C, Matsu'ura M (2013) Changes in seismic activity following the 2011 Tohoku-oki earthquake: effects of pore fluid pressure. Earth Planet Sci Lett 365:17–24. https://doi.org/10.1016/j.epsl.2013.01.017

Umino N, Matsuzawa T, Hori S, Nakamura A, Yamamoto A, Hasegawa A, Yoshida T (1998) 1996 Onikobe earthquakes and their relation to crustal structure. Zisin 51:253–264 **(in Japanese with English abstract)**

Vavryčuk V, Adamová P (2018) Detection of stress anomaly produced by interaction of compressive fault steps in the West Bohemia Swarm Region, Czech Republic. Tectonics 37:4212–4225. https://doi.org/10.1029/2018TC005163

Waldhauser F, Ellsworth WL (2000) A double-difference earthquake location algorithm: method and application to the Northern Hayward Fault, California. B Seismol Soc Am 90(6):1353–1368. https://doi.org/10.1785/012000006

Wessel P, Smith W (1998) New, improved version of generic mapping tools released. Eos Trans AGU 79(47):579

Yoshida K, Hasegawa A (2018) Sendai-Okura earthquake swarm induced by the 2011 Tohoku-Oki earthquake in the stress shadow of NE Japan: detailed fault structure and hypocenter migration. Tectonophysics 733(January):132–147. https://doi.org/10.1016/j.tecto.2017.12.031

Yoshida K, Hasegawa A, Okada T, Takahashi H, Kosuga M, Iwasaki T, Yamanaka Y, Katao H, Iio Y, Kubo A, Matsushima T, Miyamachi H, Asano Y (2014a) Pore pressure distribution in the focal region of the 2008 M7.2 Iwate–Miyagi Nairiku earthquake. Earth Planets Space 66:59. https://doi.org/10.1186/1880-5981-66-59

Yoshida K, Hasegawa A, Okada T, Iinuma T (2014b) Changes in the stress field after the 2008 M7.2 Iwate–Miyagi Nairiku earthquake in northeastern Japan. J Geophys Res: Solid Earth 119:9016–9030. https://doi.org/10.1002/2014JB011291

Yukutake Y, Honda R, Harada M, Arai R, Matsubara M (2015) A magma-hydrothermal system beneath Hakone volcano, central Japan, revealed by highly resolved velocity structures. J Geophys Res: Solid Earth 120:3293–3308. https://doi.org/10.1002/2014JB011856

Zhang H, Thurber CH (2003) Double-difference tomography: the method and its application to the Hayward Fault. California. B Seismol Soc Am 93(5):1875–1889. https://doi.org/10.1785/0120020190

Publisher's Note